A Wideband Electrical Impedance Tomography System based on Sensitive Bioimpedance Spectrum Bandwidth

A Wideband Electrical Impedance Tomography System based on Sensitive Bioimpedance Spectrum Bandwidth

Chao Tan, *Senior Member, IEEE,* Shiwei Liu, Jiabin Jia *Member, IEEE,* and Feng Dong, *Senior Member, IEEE*

***Abstract*—A wideband electrical impedance tomography system based on bioimpedance spectrum (BIS) analysis was proposed to image biological objects. The system integrated 16 electrodes to realize driving and measurement over 1 kHz - 1.1 MHz. A modified Howland current source and voltage measurement channels were designed to obtain complex impedance. Peripheral component interconnect (PCI) interface based serial data acquisition module transferred the measurement data to a host PC. The system has the least SNR of 40 dB in each channel and good consistency. The system utilized a two-step strategy, based on short time Fourier transform and Hilbert transform, the wideband chirp excitation signal was employed to analyze the BIS firstly, from which the sensitive bandwidth, i.e. the frequency range in which the amplitude (and phase angle) of the object changes rapidly, is obtained. Then, the discrete frequency points among the sensitive bandwidth were selected to compose a multi-sinusoidal signal for impedance tomography with time difference and frequency difference methods. An impedance model was tested to evaluate the performance of BIS analysis. Experiments on phantoms consisting of carrot cylinder and nylon rod were designed to verify the working strategy of the system. The results indicated that the developed system can distinguish the objects and reconstruct medium distribution with high image contrast and frequency resolution. Compared with the traditional multi-frequency electrical impedance tomography, the proposed method and system show advantages in imaging the local electrical properties with high frequency resolution and obtaining the frequency difference images in the sensitive bioimpedance spectrum bandwidth.**

***Index Terms*—Wideband, electrical impedance tomography, bioimpedance spectrum.**

I. Introduction

BIOLOGICAL tissues show distinct response under a safe electric current excitation, due to their bioelectrical impedance [1]. Based on this principle, bioelectrical impedance tomography is developed as a nonintrusive, non-radiating, compact and inexpensive visualization method [2], which aims to reconstruct the conductivity and permittivity distribution inside the biological tissue [3]–[5].

This work was supported by the National Natural Science Foundation of China (No. 61473206), The Natural Science Foundation of Tianjin (No. 17JCZDJC38400) and Science and Technology Innovation Plan of Tianjin (No.16PTSYJC00060).

Chao Tan, Shiwei Liu and Feng Dong are with Tianjin Key Laboratory of Process Measurement and Control, School of Electrical and Information Engineering, Tianjin University, Tianjin 300072, China (e-mail: tanchao@tju.edu.cn, liushiwei@tju.edu.cn; fdong@tju.edu.cn).

Jiabin Jia is with Agile Tomography Group, School of Engineering, The University of Edinburgh, Edinburgh, EH9 3JL, UK. (e-mail: jiabin.jia@ed.ac.uk)

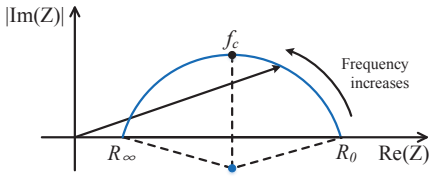

Fig. 1: Cole-Cole impedance model.

Cole-Cole impedance model depicted in Fig. 1 indicates that electrical impedance of biological tissues consists of resistive and capacitive components, which contain a wealth of biological tissue information [6]–[8]. As the frequency increases, the overall biomaterial complex impedance decreases, and the capacitive component reaches to maximum at characteristic frequency f_c. Based on BIS curves, the impedance and phase shift changed with frequency can be used to analyze the electrical characteristic of the objects [9].

Compared with BIS, electrical impedance tomography (EIT) can obtain the image of objects distribution. Traditional EIT systems, i.e., single frequency EIT (SFEIT), such as Sheffield Mark 1 and Mark 2, detected the temporal change of complex impedance at a fixed frequency, to obtain the position of the target [10]–[12]. With variety of spectral characteristic of different tissue and material, temporal change may not appear at the working frequency of SFEIT, therefore it is difficult for SFEIT to perceive and distinguish multiple objects [13]. Multi-frequency electrical impedance tomography (MFEIT) systems were developed to drive multiple frequency signals, in the form of either sequential sweep frequency sinusoidal signals or multi-sinusoidal signals [14], [15]. The research institutions around the world have done a lot of work in the past. The Sheffield Mark 3.5 MFEIT system collected data at thirty frequencies between 2 kHz and 1.6 MHz [16]. The UCLH Mark 2.5 EIT system was developed for brain imaging over 20 Hz to 256 kHz [17]. The parallel EIT system KHU Mark 2 worked in the frequency range from 10 Hz to 1 MHz [18], [19]. As another way to achieve MFEIT, linear chirp signal was used in wideband EIT to obtain temporal phase and amplitude shift [20]. Additionally, 3D impedance images were also reconstructed to obtain specific spatial location using multiple planes of electrodes [21]. In MFEIT, time difference (TD) images can be reconstructed at each independent frequency referring to the corresponding full homogeneous filed [22]. Frequency difference (FD) images

are reconstructed from different frequency response data with a single frequency data as a reference. Compared with TD method, FD allows to image the target without the knowledge of a prior condition [23]–[26].

Bioimpedance theory indicates that there is a diversity on biospectrum properties of different biological materials. FD imaging can achieve better results when each desired frequency, at which a FD image is created, exists in sensitive bandwidth of BIS. The selection of reference frequency also affects the image results. Traditional MFEIT systems drive different objects with fixed multi-frequency scheme, lacking of targeted excitation on the specific object, due to the unknown BIS. In addition, high bandwidth and high frequency resolution cannot be improved simultaneously. Taking 1MHz (bandwidth) and 10kHz (resolution) as an example, 100 frequency points are required. Considering the system design and signal to noise ratio, traditional MFEIT is unable to meet the above requirements, using whether sequential sweep or multi-sinusoidal signals. Therefore, high quality image reconstruction results are not guaranteed in MFEIT in some cases.

Therefore, this paper presents a wideband electrical impedance tomography system based on sensitive bioimpedance spectrum bandwidth (SWEIT). Given the different excitation configuration, the SWEIT system can generate wideband chirp signals and adaptive multi-sinusoidal signals. The SWEIT system adopts the two-step strategy: analyze the spectral characteristics to obtain the BIS curve using wideband signal firstly, and determine the sensitive bandwidth, i.e. selecting the frequency interval in which the electrical characteristics change quickly and significantly. Then configure the desired frequency components at the sensitive bandwidth to compose a multi-sinusoidal signal for multi-frequency tomography. In FD image reconstruction based on BIS analysis, the start or stop frequency of sensitive bandwidth is used as the reference frequency for image reconstruction. The electrical characteristics difference between the reference frequency and desired frequency, and among desired frequencies are obvious and considerable, which helps reconstructing images with high color contrast. Linear chirp signal over 1 kHz to 1.1 MHz was used to obtain the BIS, i.e., amplitude-frequency and phase-frequency characteristics are analyzed with short-time Fourier transform (STFT) and Hilbert transform on the response voltage. Then, customized multi-sinusoidal signals are applied to obtain TD and FD images. The impedance and phase shift in each frequency were extracted utilizing quadrature demodulation.

This paper is organized as following: Section II introduces the design of FPGA based hardware system, signal demodulation and image reconstruction. Performance test and image experiment were conducted with carrot cylinder and nylon rod, and the TD and FD images were reconstructed at selected frequencies, which are demonstrated in the Section III (RESULT) in detail. In the Section IV (CONCLUSIONS), the beneficial effect and future work are discussed.

II. METHOD

A. System Architecture

The proposed SWEIT system in Fig. 2 consists of three parts: (i) electrode-array, (ii) a Field Programmable Gate Array (FPGA) based printed circuit board (PCB), compatible with Peripheral Component Interconnect (PCI) protocol, including a single channel constant current excitation source (CCES) and dual voltage measurement channels, which are embedded into host PC, (iii) host PC for data acquisition and image reconstruction. The SWEIT system is shown in Fig. 3.

B. Excitation-Measurement strategy

As a frequency dependent function, the bioimpedance Z_f of object can be represented as:

$$Z_f = R_f - jX_f \tag{1}$$

$$Z_f = \frac{V_m}{I_e} = \frac{V\sin(2\pi ft \pm \varphi)}{I\sin(2\pi ft)} = \frac{|V|\angle \pm \varphi}{|I|} = |Z|\angle \pm \varphi \tag{2}$$

where R_f is the real part of complex impedance Z_f, while X_f is the imaginary part. V_m is the measured voltage signal, and I_e is the excitation current signal. V, I, $|Z|$ and φ are the amplitude of V_m and I_e, norm of impedance and phase shift respectively [27], [28]. The objects under testing are imaged with complex transfer impedance ($|Z|$) and phase shift (θ) respectively, which are analyzed from the boundary voltage (V_m) developed by the constant current (I_e).

EIT system employs adjacent drive and receive electrodes combinations in four-electrode technique, as shown in Fig. 4, which can reduce the effect of contact impedance between electrodes and phantom on the measured voltage signal [29]. A constant current is excited through two excitation electrodes, and the voltage between another two electrodes can be measured. Note that the dotted lines in the figure represent the equipotential, vertical with the electric field line generated by excitation current.

C. Sensors

There are two types of front sensors of SWEIT system. Two Stainless steel electrodes connected with four coaxial cables depicted in Fig. 5a make up the impedance spectrum analysis sensor (SAS), with length 100mm, width 30 mm and height 30 mm. The cylindrical tank connected with 16 coaxial cables shown in Fig. 5b is tomography sensor (TS), with diameter 125 mm and height 30 mm.

The presented SWEIT system can address 16 electrodes to TS through the analog multiplexer switch. With the logic and timing control from FPGA, the system can realize the excitation and measurement, traversing all electrodes in TS. In BIS analysis mode, the four electrodes utilized in SAS are connected to the 1-4 channels of multiplexers. Additionally, in order to reduce the influence of parasitic capacitances on bioelectrical impedance, the multiplexers with low capacitance are used and the voltage buffers following all measurement electrodes are designed.

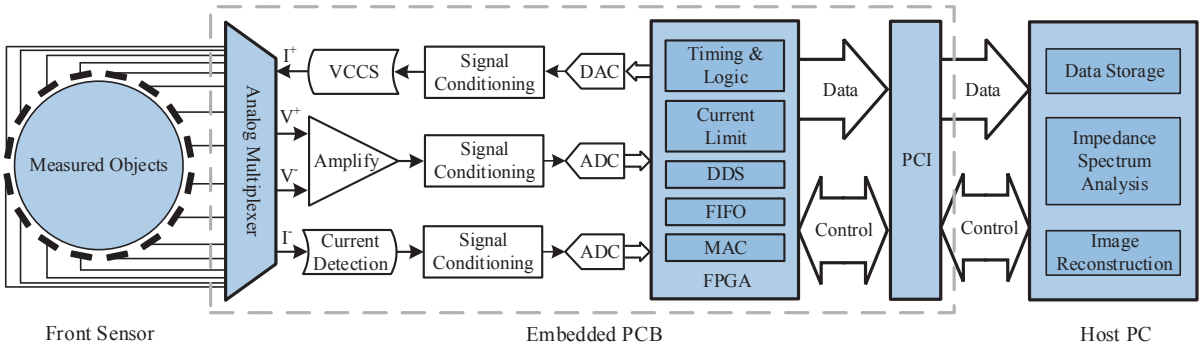

Fig. 2: The architecture of the developed SWEIT system.

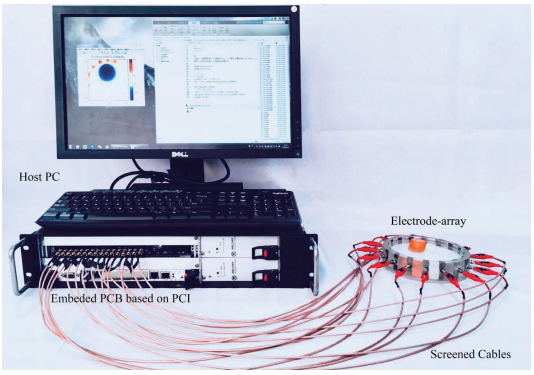

Fig. 3: Developed SWEIT System.

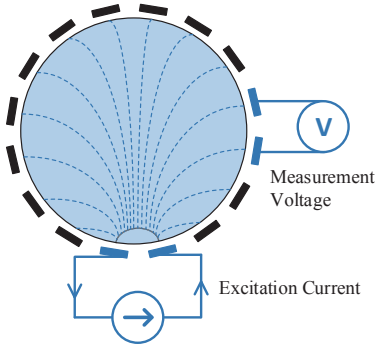

Fig. 4: Adjacent drive and measuring strategy based on four-electrode technique.

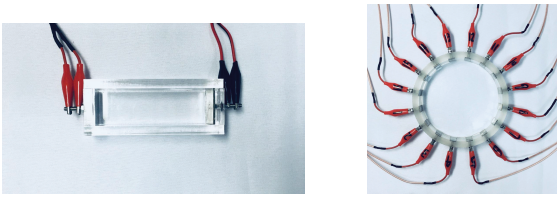

(a) (b)

Fig. 5: The front sensors of SWEIT system. (a) Impedance spectrum analysis sensor (SAS). (b) Cylindrical bioimpedance tomography sensor (TS).

The excitation-and-measurement module and sensor are connected by coaxial cables with length of 1 m, aiming to eliminate the crosstalk between cables, and reduce the noise from external environment. The characteristic impedance of coaxial cable is 50 Ω, conductor and insulation diameters are 1.07 mm and 3.05 mm, respectively, and the parallel capacitance is 85 pF/m.

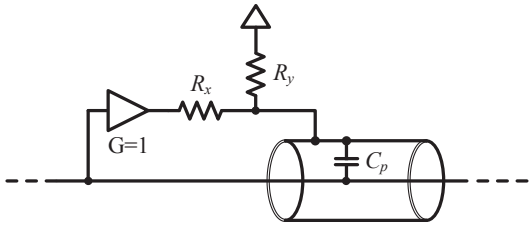

Fig. 6: Shield is driven with core voltage.

Driven shield is adopted on coaxial cables depicted in Fig. 6. Measurement voltage is driven to shield to keep the potential balance and prevent shunting through C_p. Additionally, to avoid self-oscillation at positive feedback path, serial resistance R_x and R_y are placed to divide voltage.

D. Configurable Current Excitation Source

The CCES is mainly composed of configurable direct digital synthesis (DDS) module and voltage controlled current source (VCCS) module. The SWEIT system is allowed to configure two excitation strategies, i.e. wideband chirp signal and multi-sinusoidal signal. Also, the amplitude of CCES can be adjusted adaptively under different multi-frequency excitation conditions.

1) Configurable DDS: The basic principle of DDS is shown in Fig. 7. The desired frequency f_d is set by the value of the phase increment $\Delta\theta$ and can be calculated from

$$f_d = \frac{f_{clk}}{M} \cdot \Delta\theta \tag{3}$$

where M is the number of discrete points in one sinusoidal cycle. The phase-to-amplitude transformation is achieved through lookup tables [30]. The digital amplitude signals are converted to analog signal through a 14-bit DAC and a low-pass filter with a cut-off frequency of 1.8 MHz.

Fig. 8 depicts the five-channel configurable DDS module in SWEIT system. Based on the same ROM, wideband chirp

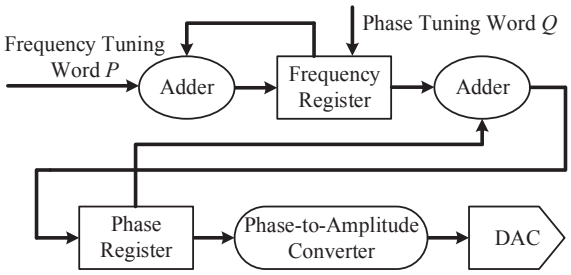

Fig. 7: The schematic of Direct Digital Synthesis.

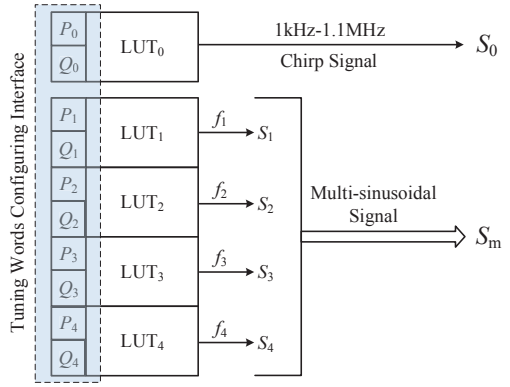

Fig. 8: Five-channel configurable DDS module.

signal and multi-sinusoidal signal are generated according to different $\Delta\theta$. P_i (i=0, 1, 2, 3, 4) and Q_i are control words, which can be configured flexibly to determine the desired frequency in practical work. Four single frequency signals can be synthesized into a multi-frequency excitation signal, which can guarantee the ratio of signal-to-noise (SNR), and the response signal demodulation implemented in FPGA. Compared with the existing systems [16], [17], the proposed DDS module can modify frequency components by means of control word port quickly, while the common is fixed multi-sinusoidal signal, without adjustable bandwidth and frequency resolution.

2) Output Current Safety Limit: The constant current is generated using classic Howland voltage controlled current source circuit, based on which a programmable gain amplifier is employed to adjust the control voltage of VCCS module, to change the current amplitude adaptively.

The amplitude of CCES is limited by IEC 60601-1 medical electrical equipment standard. Considering the personal safety, the maximum auxiliary current applied should less than the $0.1\times f_e$ mA rms, where f_e is the excitation frequency (kHz), with the upper limit of 10 mA rms [31]. Compatible with IEC 60601-1 standard, the amplitude of chirp signal CCES is 1mA, and the amplitude of multi-sinusoidal signal CCES is $0.1\times f_{em}$ mA, where the fem is the minimum frequency (kHz) in multi-frequency signal S_m.

E. Dual Voltage Measurement Modules

Dual voltage measurement modules are developed to detect the voltage across the unknown impedance and the potential drop over the reference resistance simultaneously. Even the designed CCES has high output impedance, there is a fluctuation in the output current as the load changes, which will cause impedance calculation error if using constant value. A 100 Ω (0.01% accuracy) reference resistance is set in series with current output port to provide reference voltage, which is used to obtain the amplitude and phase of CCES synchronously, aiming to calibrate unknown impedance measurement results and provide reference for phase shift analysis. More importantly, the system can monitor the auxiliary current in real time, and cut off CCES to stop system work actively.

The same voltage buffers, instrumentation amplifiers, variable gain amplifiers (VGA), filter circuit, and ADC are set at each module. The gain of VGA is adjusted digitally to accommodate the full dynamic range of ADC, and to improve the signal-to-noise ratio (SNR).

F. Signals Demodulation Scheme

1) Chirp Signal: Chirp response and reference voltage signals are converted to digital signal respectively, and sent to the host PC directly, where demodulated to obtain BIS. Based on STFT, performing time-frequency analysis on temporal discrete signal, impedance-frequency characteristic curve can be draw with frequency resolution of 1 kHz. On the other hand, Hilbert transform is conducted to obtain the phase-frequency information of objects. Further, relative phase shift change with frequency is calculated, referring to the voltage over reference resistance. The two results are given by the following formulas:

$$|Z| = \frac{V_{un}}{V_{ref}} \cdot R_{ref} \tag{4}$$

$$\Delta\theta = \varphi_{un} - \varphi_{ref} \tag{5}$$

where V_{un} and V_{ref} are the voltage over the unknown impedance and the voltage over the reference resistance respectively, while $|Z|$ and R_{ref} represent the calculated unknown impedance and the value of reference resistance, respectively. $\Delta\theta$, φ_{un}, and φ_{ref} are the phase shift, phase angle analyzed from the unknown and reference impedance, respectively. In order to reduce the edge effects of numerical analysis methods, the resulting BIS is limited in the range from 10 kHz to 1 MHz.

2) Multi-sinusoidal Signal: Multi-sinusoidal signals are demodulated with FPGA based hardware algorithm. Corresponding to the dual voltage measurement modules, there are two separate pre-processing and demodulation units. Before entering the MAC, the signals to be demodulated will be digitally filtered to eliminate the glitch and improve the SNR. In addition, frequency dependent offset voltage exists due to the capacitive effect during switching. The signals in each measurement channel are truncated several cycles in the beginning of one acquisition, until the response signals recover to steady state. After the above pre-processing, the signals are sent to demodulation units.

Digital quadrature demodulation is implemented in FPGA to demodulate the impedance and phase shift from multi-sinusoidal response signals in real time. Sampled by 40 MHz

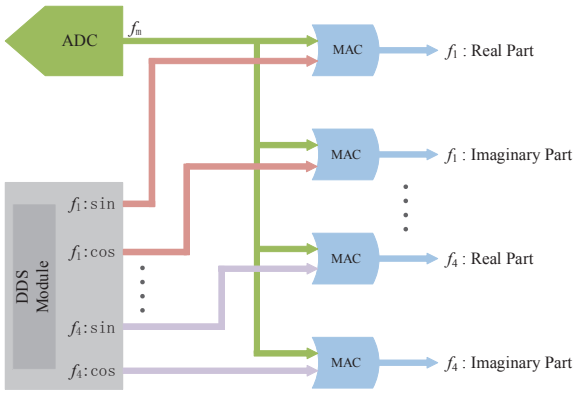

Fig. 9: Quadrature demodulation schematic.

ADC, analog voltage response signal of a certain frequency can be discretized as

$$S_r(n) = A_r \sin(2\pi \cdot \frac{n}{N} + \theta_r) \tag{6}$$

where A_r represents the amplitude of signal, while θ_r is the phase of the signal. n and N denote the nth and total number of sampling points, respectively. Based on the multiply accumulation (MAC) unit compiled in FPGA, as shown in Fig. 9, the quadrature demodulator computes the in-phase and quadrature components as follows:

$$I_s = \frac{2}{N} \sum_{n=0}^{N-1} \sin\left(2\pi \cdot \frac{n}{N}\right) \cdot S_r(n) = A_r \cos(\theta_r) \tag{7}$$

$$Q_s = \frac{2}{N} \sum_{n=0}^{N-1} \cos\left(2\pi \cdot \frac{n}{N}\right) \cdot S_r(n) = A_r \sin(\theta_r) \tag{8}$$

where I_s and Q_s are the in-phase and quadrature component, i.e. real part and imaginary part of the signal. Solving the equations (7) and (8), amplitude and phase can be calculated by

$$A_r = \sqrt{I_s^2 + Q_s^2} \tag{9}$$

$$\theta_r = \arctan \frac{Q_s}{I_s} \tag{10}$$

G. Data Acquisition and Image Reconstruction

The SWEIT system is designed to meet the PCI protocol, and can be embedded in host PC, which makes the system compact. Meanwhile, the electric power from PC is transmitted to the system with hardware-level isolation, which ensures human safety. Compliant with the PCI version 2.2, based on data pipe architecture and scatter/gather DMA, 32-bit local data is transferred to PCI at 50 MHz. As depicted in Fig. 10, host PC completes three tasks: data saving, information extraction and visualization. Developed using C++ language, data acquisition and storage software controls the procedure and saves data to hard disk.

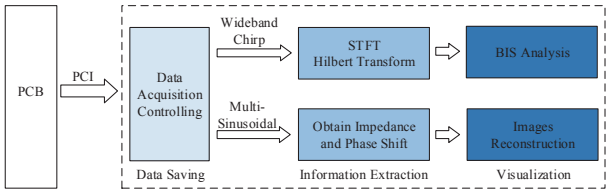

Fig. 10: Data acquisition and image reconstruction on host PC.

Tikhonov regularization algorithm was used to solve the ill-posed problem, and images can be estimated as the following formula

$$x = (J^T J + \lambda I)^{-1} J^T b \tag{11}$$

where J and J^T are the Jacobian matrix and its transpose matrix, respectively. λ and I are the regularization coefficient and identity matrix, respectively. b is the boundary voltage. Based in same λ, the inhomogeneous objects are visualized at each of desired frequencies, and the final image has a resolution of 200px×200px. The sensor with 16 electrodes was used in the imaging experiment, 208 data (16 excitation modes corresponding with 13 measurement modes, respectively) were acquired to reconstruct one frame image. TD and FD images were obtained, taking the homogeneous field at same frequency and the inhomogeneous field at desired frequency as the reference, respectively.

III. Results

A. Performance Evaluation of CCES

Performance of CCES is mainly decided by controlling voltage and circuit configuration of VCCS. The quality of analog voltage is limited in amplitude quantization (data width) and sampling points (data depth), especially for high frequency. Processed with differential amplification and band-pass filtering, the resulting linear chirp signal scoped in oscilloscope with the bandwidth of 1 kHz - 1.1 MHz is shown in Fig. 11, and the duration of 1ms. The amplitude-frequency characteristic indicates that 1.7 MHz out-of-band noise is attenuated 40 dB, as well as fitting and flat shape of spectrum. The multi-sinusoidal signal consists of four single-frequency components, as the example depicted in Fig. 12, which include 50 kHz, 100 kHz, 200 kHz and 400 kHz.

The high-quality CCES is demanded to drive unknown impedance in EIT system. The modified Howland current source is a classical scheme applied in CCES [32]. High-precision matching resistors with ±0.01% tolerance were used in Howland circuit. Limited gain bandwidth product of amplifier and parasitic capacitance restrain the output performance to a certain extent. Output current test under different frequency and load was carried out, as presented in Fig. 13. When the load is less than 2.6 kΩ, the output current remains constant below 500 kHz. At the maximum load 4 kΩ, the output current is 4.825 mA with the deviation of 3.5%. Fig. 13b shows the output current value measured at different excitation frequencies at 1.5 kΩ load. When the excitation frequency is 1 MHz, the output current reduces to 4.813 mA with the deviation of 3.74%. In conclusion, drive performance

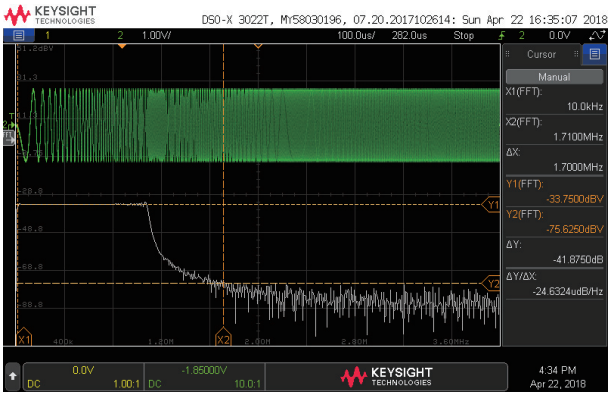

Fig. 11: Wideband chirp signal and frequency spectrum analysis based on FFT.

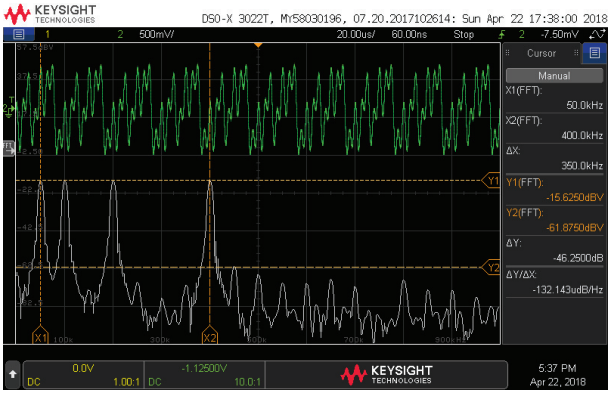

Fig. 12: An example of multi-sinusoidal signal (composed of 50 kHz, 100 kHz, 200 kHz and 400 kHz) and spectrum.

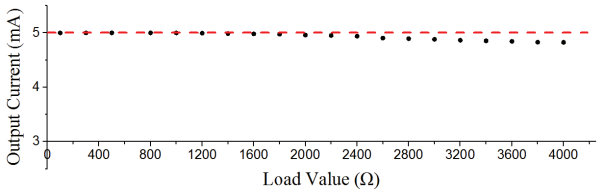

(a)

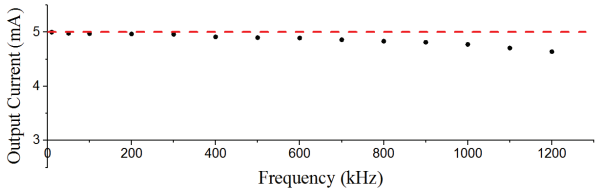

(b)

Fig. 13: CCES output performance test results. (a) Output current value measured at different loads. (b) Output current value measured at different frequencies.

is weakened inevitably when excitation frequency and load increases, but current source has a good constant current output within a certain range.

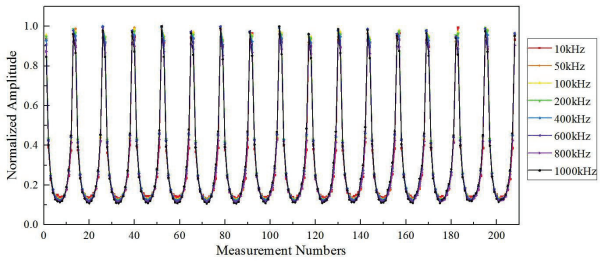

Fig. 14: The consistency of channel at the tested frequencies.

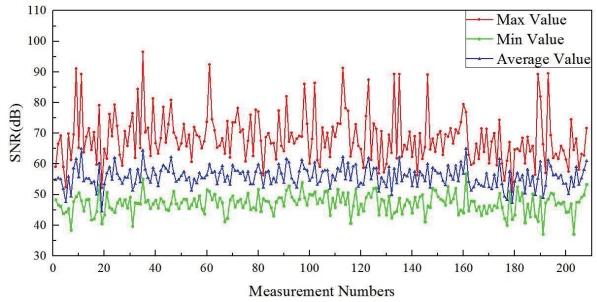

Fig. 15: SNR of all 208 measurement channels at the tested frequencies.

B. The Consistency of Channel

Ideally, at different excitation, the boundary response voltage at same relative position is consistent under the homogeneous object. The boundary voltage was calculated at all 208 measurement channels at 10 kHz, 50 kHz, 100 kHz, 200 kHz, 400 kHz, 600 kHz, 800 kHz, 1000 kHz. The raw data was collected from the TS with 0.1% w/v saline water, and the result of the consistency is shown in Fig. 14. At the tested frequencies, the tendency of boundary response voltage in 16 different excitation patterns is consistent.

C. Signal-to-Noise Ratio

The SNR was calculated based on the similar experimental condition of the consistency testing. The SNR in each measurement channel was analyzed as the following equation:

$$SNR = 10\lg \frac{\sum_{i=1}^{N} \bar{A}^2}{\sum_{i=1}^{N} (A_i - \bar{A})^2} \tag{12}$$

where the N is the experiment times at single channel at a certain frequency, and N=500. A_i and $\bar{A}$ are the ith measurement value and the mean of all measurement, respectively. The result of SNR is shown in Fig. 15, in which maximum, minimum, and average values of 208 channels were calculated from the values at each of above frequencies. The average SNR of the system is 56 dB.

D. Bioimpedance Spectrum Analysis

Based on the wideband chirp signal and SAS, a R+R||C impedance model and the carrot cylinder were connected

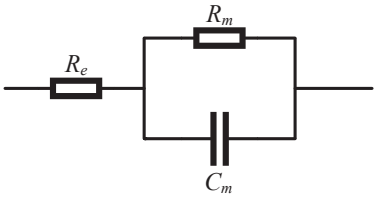

Fig. 16: R+R||C three elements impedance loads. $R_e = 400.4\ \Omega$, $R_m = 1646.0\ \Omega$, $C_m = 1$ nF.

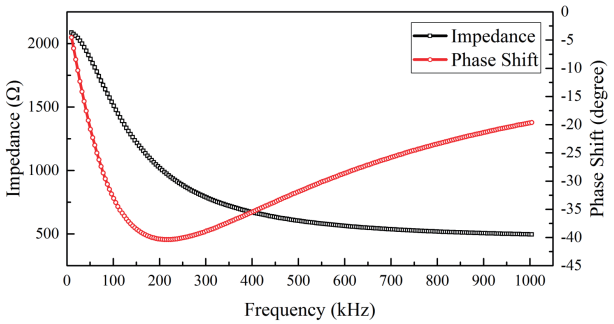

Fig. 17: Complex impedance and phase shift of R+R||C model. Data from impedance analyzer Keysight 4294A.

to the SWEIT system. To verify the accuracy of the result from proposed system, the data collected from a commercial precision impedance analyzer (4294A, Keysight Technologies) was used as the reference.

The R+R||C three element impedance model represented in Fig. 16 was set up in the experiment. The real value of the passive components was measured with 0.01% uncertainty, $R_e = 400.4\ \Omega$, $R_m = 1646.0\ \Omega$, $C_m = 1.0$ nF. The BIS measured from the impedance analyzer is shown in the Fig. 17. Applying the STFT, the impedance spectrum and the phase spectrum were depicted in Fig. 18. It was observed that the impedance-frequency characteristic was consistent between impedance analyzer and SWEIT, and the maximum impedance error was 1.47% at various frequencies. On the other hand, the absolute phase shift of two sets of data was different, but the relative change over frequency was consistent. The absolute phase maximum error was 24.8%, while the relative maximum error was 3.11%. The phase-frequency curve from SWEIT was offset a certain phase, which was the difference of average phase at various frequencies between the impedance analyzer and the SWEIT. Then the relative result was calculated using the original data of impedance analyzer and the offset value of SWEIT.

Further, the biological sample, taking the carrot cylinder as an example, was tested to evaluate the performance using SAS, as shown in Fig. 19. The impedance analyzer result was shown in Fig. 20, and the SWEIT system result was shown in Fig. 21. The absolute maximum impedance error was 1.66%, and the relative maximum phase error was 4.08%. The absolute phase shift results obtained from the two methods were different, which may be caused by measuring cables and fixed clamps connected with SAS, which were different with impedance analyzer in electrical characteristic, and multiplexers in SWEIT

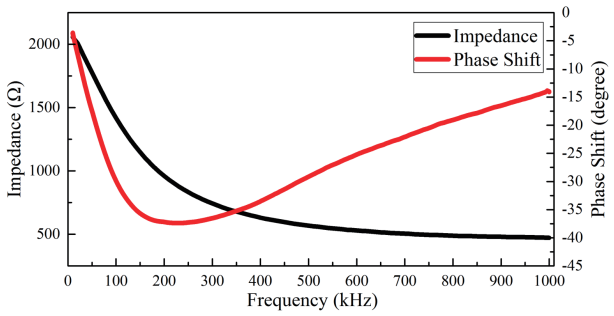

Fig. 18: Complex impedance and phase shift of R+R||C model based on Hilbert transform. Data from SWEIT.

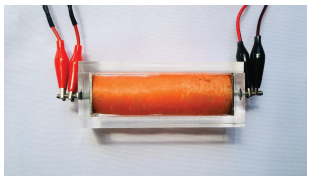

Fig. 19: The carrot cylinder was tested to evaluate the performance using SAS.

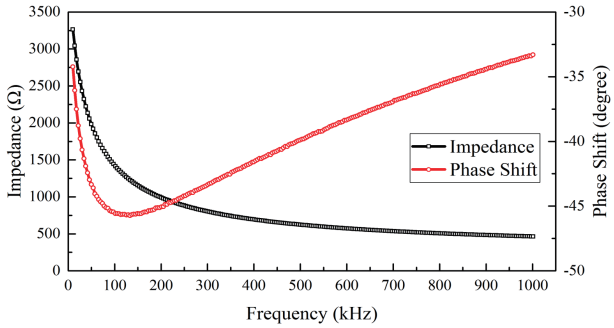

Fig. 20: Complex impedance and phase shift of carrot cylinder. Data from impedance analyzer Keysight 4294A.

had inherent phase shift. But there was no effect on analyzing the relative change to determine the sensitive bandwidth, and then no need to perform specialized calibration for phase shift.

Comparing the BIS measured by two devices, same performance conclusion can be draw with the R+R||C model. When the frequency was less than 200 kHz, the impedance changed with frequency drastically, and then the trend tended to be flat. Additionally, there were significant phase changes before and after 100 kHz. Based on SWEIT, the BIS of the vegetables can be obtained, and sensitive bandwidth was also analyzed from the characteristic curve.

E. Imaging Experiment

The imaging experiment was conducted in the TS with 16 electrodes. To improve the result of the reconstructed images, the 0.1% w/v salt solution was formulated as the homogeneous object. The impedance and phase of salt solution is independent with frequency nearly, which does not affect image reconstruction. The carrot cylinder and nylon rod were used as inhomogeneous objects to realize TD and FD images.

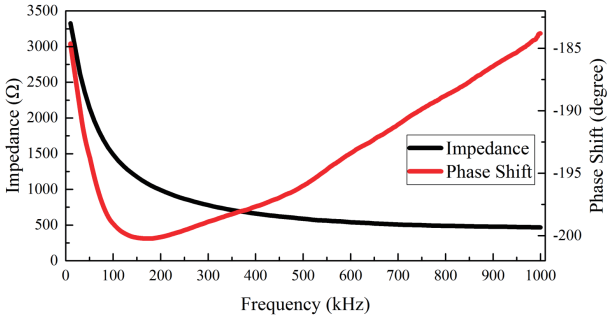

Fig. 21: Complex impedance and phase shift of carrot cylinder based on Hilbert transform. Data from SWEIT.

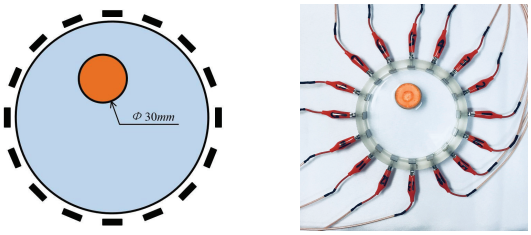

(a) (b)

Fig. 22: Phantom A: a single carrot cylinder with diameter of 30mm was placed at the TS, located near electrodes 5 and 6. (a) geometric distribution, (b) actual experiment situation.

A single carrot cylinder with diameter of 30 mm was placed at the TS (Phantom A). The distribution location and size are represented in Fig. 22, in which the subgraph (a) shows the geometric distribution, while the subgraph (b) shows the actual experiment situation. Note that the carrot cylinder used in imaging experiment is same with the one tested in bioimpedance spectrum analysis.

According to the impedance and frequency spectrum characteristics depicted in Fig. 21, collected from SWEIT. 10 kHz - 200 kHz for impedance and 200 kHz - 1000 kHz for phase were selected as the sensitive bandwidth, respectively. In impedance images reconstruction, 10 kHz, 20 kHz, 40 kHz, 70 kHz, 100 kHz, 130 kHz, 160 kHz, and 200 kHz were synthesized as two multi-sinusoidal excitation signals. In phase shift images reconstruction, 300 kHz, 400 kHz, 500 kHz, 600 kHz, 700 kHz, 800 kHz, 900 kHz, and 1000 kHz were synthesized as two multi-sinusoidal excitation signals. These single frequency components were distributed in sensitive bandwidth typically, and the difference of response voltage at them can reflect the changes in electrical characteristics of carrot cylinder under test obviously.

Fig. 23 displays the TD impedance and phase images at eight frequencies, and the response voltage from the homogeneous object in each of frequencies were selected as the reference. In TD impedance and phase images reconstruction, the carrot cylinder was visualized in respective sensitive bandwidth, and the imaging performance got poor with increasing frequency, because of the decreasing contrast between the background solution and the objects.

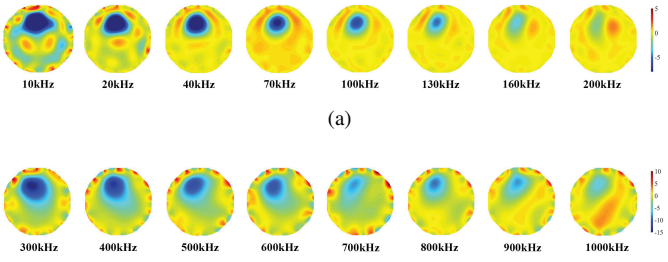

(a)

(b)

Fig. 23: Time difference images of phantom A, referring to the homogeneous phantom at corresponding frequency. (a) TD impedance images at sensitive bandwidth 10 kHz - 200 kHz, (b) TD phase shift images at sensitive bandwidth 300 kHz - 1000 kHz. Color bar is unified scale for this series of images.

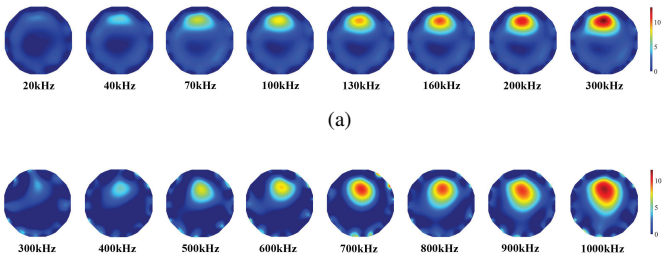

(a)

(b)

Fig. 24: Frequency difference images of phantom A. (a) FD impedance images with 10 kHz as the reference, (b) FD phase shift images with 200 kHz as the reference. Right color bar is unified scale for this series of images.

Compared with the TD method, FD is more practical because no reference data obtained from the homogeneous phantom. Based on the selected bandwidth, the start frequency 10 kHz and 200 kHz were selected as the reference for FD impedance and phase shift images, respectively, as shown in Fig. 24. The same scale of color bar was adopted in two set of FD images. The significant change from reference frequency to desired frequency improved the quality of FD images. The distribution of the carrot cylinder became clear at high frequency.

According to the phase-frequency spectrum in Fig. 21, the phase shift increased first and then decreased in the frequency range from 70kHz to 230kHz. The time difference phase shift images at 70kHz, 100kHz, 130kHz, 160kHz, 200kHz, and 230kHz are reconstructed in Fig. 25, from which the distribution of the target and the minor changes of the electrical characteristics can be presented using a set of images in the narrow band. However, the traditional MFEIT images the phantom in the fixed frequencies, such as 10kHz, 100kHz, 200kHz, ,1000kHz, and the frequency resolution is low. Therefore, some local changes of the electrical characteristics happened at the 100kHz bandwidth are not revealed in the above example of MFEIT. Based on the SWEIT, multi-frequency signal can be configured adaptively and densely to focus on the desired bandwidth with high frequency resolution.

In Fig. 24a, the satisfactory FD impedance images were

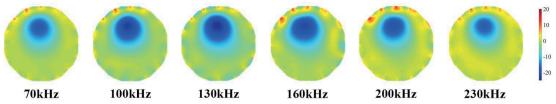

Fig. 25: TD phase shift images of phantom A in 70kHz - 230kHz, referring to the homogeneous phantom at corresponding frequency. Right color bar is normalized scale for this series of images.

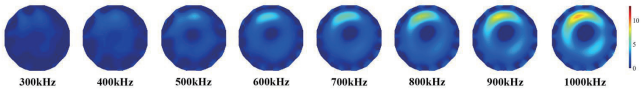

Fig. 26: FD impedance images of phantom A in 300kHz - 1000kHz, with 200 kHz as the reference. Right color bar is unified scale for this series of images.

obtained in 10 kHz - 300 kHz. Due to the lack of spectrum information and fixed excitation strategy, the traditional MFEIT is incompetent to obtain good results under any condition. When a MFEIT system excited the designed phantom A at 200kHz, 300kHz, 400kHz, 500kHz, 600kHz, 700kHz, 800kHz, 900kHz, and 1000kHz, its FD impedance images are shown in Fig.26. Comparing Fig. 24a and Fig. 26, the image reconstruction results are deteriorated in between 300kHz and 1000kHz, since the complex impedance is almost constant over frequency. The electrical impedance tomography based on the sensitive spectrum bandwidth has clear advantages over the traditional MFEIT.

Further research was conducted for two objects, i.e. a carrot cylinder (diameter 25 mm) and a nylon rod (diameter 30 mm) were placed at the TS (Phantom B). The distribution location and size are represented in Fig. 27, in which the subgraph (a) shows the geometric distribution, while the subgraph (b) shows the actual experiment situation. Fig. 28 shows the TD impedance and phase shift images of phantom B. In TD impedance image reconstruction, the location of the nylon rod was clear at each frequency, while the location was invisible completely in phase shift images. The reason is that impedance difference between nylon and homogeneous was always great and almost unchanged within the range of frequency applied, but no phase shift occurred on nylon. In contrast, whether in TD impedance or phase shift images, the location of the carrot cylinder became blurred with increasing frequency, due to frequency dependent impedance and phase shift existed on carrot, which were same with the TD images of phantom A in tendency. The FD impedance and phase shift images are shown in Fig. 29, the location of the carrot cylinder became clear with increasing frequency, while the nylon rod is not captured throughout various frequencies. As an almost purely resistive target, the impedance of nylon rod does not change with frequency, and no phase shift occurs at each frequency, therefore the nylon rod is not found in FD images.

Whether TD or FD impedance images, two inhomogeneous objects with different BIS properties could be identified, and

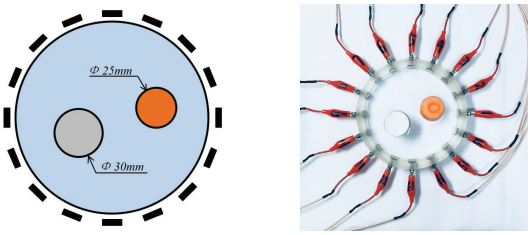

(a) (b)

Fig. 27: Phantom B: a carrot cylinder (diameter 25 mm, marked in orange) and a nylon rod (diameter 30 mm, marked in gray) were placed at the TS. (a) geometric distribution, (b) actual experiment situation.

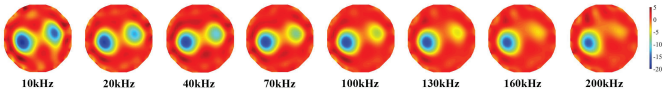

(a)

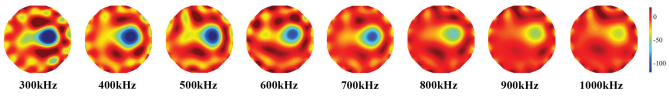

(b)

Fig. 28: Time difference image reconstruction results of phantom B. (a) TD impedance images with the homogeneous phantom at corresponding frequency as the reference, (b) TD phase shift images with the homogeneous phantom at corresponding frequency as the reference. Right color bar is unified scale for this series of images.

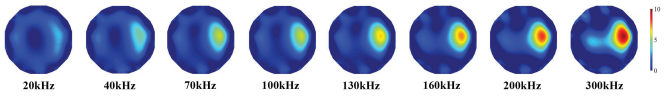

(a)

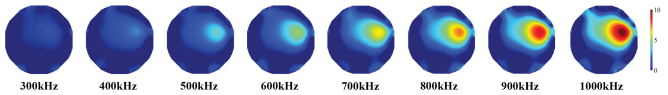

(b)

Fig. 29: Frequency difference image reconstruction of phantom B. (a) FD impedance images with 10 kHz as the reference, (b) FD phase shift images with 200 kHz as the reference. Right color bar is unified scale for this series of images.

the objects with changed electrical properties can be located. Additionally, the BIS characteristics of them were reflected in distribution images. Note that the preferred sensitive bandwidth guaranteed the quality of every image reconstruction, especially in FD.

IV. Conclusion

A wideband electrical impedance tomography system based on impedance spectrum analysis was developed, it is compatible with PCI protocol and embedded into host PC, which made

the system compact. Based on FPGA, wideband chirp and configurable multi-sinusoidal signal were generated to drive objects under test. Dual-voltage measurement channels were designed to provide reference for calculating the impedance and phase shift. The chirp response signal was analyzed to obtain the sensitive bandwidth on host PC, and determine the multi-frequency components used in tomography. As the prior knowledge, the BIS information makes the choice of multi-frequency components more targeted and effective.

Based on carrot cylinder and nylon rod, SWEIT system was used to carry out the images experiment. TD and FD images were reconstructed with impedance and phase shift, respectively. In addition, the tradition MFEIT and the proposed SWEIT were compared to indicate the improved quality and validity on imaging the location of the targets in the sensitive wide and narrow bandwidth, benefited from the high frequency resolution and adjustable excitation frequency. Future work will focus on imaging in real time, as well as broadening the system application to phantom based on body model and actual clinical medical symptoms.

REFERENCES

[1] D. C. Barber, B. H. Brown, and I. L. Freeston, "Imaging spatial distributions of resistivity using applied potential tomography-APT," in *Information Processing in Medical Imaging*, F. Deconinck, Ed. Dordrecht: Springer, 1983, pp. 446–462.

[2] T. K. Bera and J. Nagaraju, "A multifrequency electrical impedance tomography (EIT) system for biomedical imaging," in *International Conference on Signal Processing and Communications*, 2012, pp. 1–5, doi: 10.1109/SPCOM.2012.6290216.

[3] Z. Szczepanik and Z. Rucki, "Frequency analysis of electrical impedance tomography system," *IEEE Transactions on Instrumentation and Measurement*, vol. 49, no. 4, pp. 844–851, 2000, doi: 10.1109/19.863936.

[4] A. P. Bagshaw, A. D. Liston, R. H. Bayford, A. Tizzard, A. P. Gibson, A. T. Tidswell, M. K. Sparkes, H. Dehghani, C. D. Binnie, and D. S. Holder, "Electrical impedance tomography of human brain function using reconstruction algorithms based on the finite element method," *NeuroImage*, vol. 20, no. 2, pp. 752–764, 2003, doi: 10.1016/S1053-8119(03)00301-X.

[5] B. H. Brown, D. C. Barber, W. Wang, L. Lu, A. D. Leathard, R. H. Smallwood, A. R. Hampshire, R. Mackay, and K. Hatzigalanis, "Multi-frequency imaging and modelling of respiratory related electrical impedance changes," *Physiological Measurement*, vol. 15 Suppl 2a, pp. A1–A12, 1994, doi: 10.1088/0967-3334/15/2A/001.

[6] K. S. Cole and R. H. Cole, "Dispersion and absorption in dielectrics I. Alternating Current Characteristics," *The Journal of Chemical Physics*, vol. 9, no. 4, pp. 341–351, 1941, doi: 10.1063/1.1750906.

[7] H. Griffiths, "A cole phantom for EIT," *Physiological Measurement*, vol. 16, no. 3 Suppl A, pp. A29–A38, 1995, doi: 10.1088/0967-3334/16/3A/003.

[8] M. R. Baidillah, A. A. S. Iman, Y. Sun, and M. Takei, "Electrical impedance spectro-tomography based on dielectric relaxation model," *IEEE Sensors Journal*, vol. 17, no. 24, pp. 8251–8262, 2017, doi: 10.1109/JSEN.2017.2710146.

[9] F. Seoane, R. Bragos, and K. Lindecrantz, "Current source for multi-frequency broadband electrical bioimpedance spectroscopy systems. a novel approach," in *International Conference of the IEEE Engineering in Medicine and Biology Society*, New York, NY, USA, 2006, pp. 5121–5125, doi: 10.1109/IEMBS.2006.259566.

[10] D. S. Holder and A. Khan, "Use of polyacrylamide gels in a saline-filled tank to determine the linearity of the sheffield mark 1 electrical impedance tomography (EIT) system in measuring impedance disturbances," *Physiological Measurement*, vol. 15, no. 2A, pp. A45–A50, 1994, doi:10.1088/0967-3334/15/2A/006.

[11] K. Boone, A. M. Lewis, and D. S. Holder, "Imaging of cortical spreading depression by eit: implications for localization of epileptic foci," *Physiological Measurement*, vol. 15 Suppl 2a, pp. A189–A198, 1994, doi: 10.1088/0967-3334/15/2A/024.

[12] W. Wang, B. H. Brown, and D. C. Barber, "Performance of the sheffield Mk3A multi-frequency system for electrical impedance tomography," in *IEE Colloquium on Innovations in Instrumentation for Electrical Tomography*, London, UK, 1995, pp. 10–11, doi: 10.1049/ic:19950645.

[13] R. J. Yerworth, R. H. Bayford, B. Brown, P. Milnes, M. Conway, and D. S. Holder, "Electrical impedance tomography spectroscopy (EITS) for human head imaging," *Physiological Measurement*, vol. 24, no. 2, pp. 477–489, 2003, doi: 10.1088/0967-3334/24/2/358.

[14] M. Nahvi and B. S. Hoyle, "Electrical impedance spectroscopy sensing for industrial processes," *IEEE Sensors Journal*, vol. 9, no. 12, pp. 1808–1816, 2009, doi: 10.1109/JSEN.2009.2030979.

[15] T. I. Oh, E. J. Woo, and D. Holder, "Multi-frequency EIT system with radially symmetric architecture: KHU Mark1," *Physiological Measurement*, vol. 28, no. 7, pp. S183–S196, 2007, doi: 10.1088/0967-3334/28/7/S14.

[16] A. J. Wilson, P. Milnes, A. R. Waterworth, R. H. Smallwood, and B. H. Brown, "Mk3.5: a modular, multi-frequency successor to the Mk3a EIS/EIT system," *Physiological Measurement*, vol. 22, no. 1, pp. 49–54, 2001, doi: 10.1088/0967-3334/22/1/307.

[17] A. McEwan, A. Romsauerova, R. Yerworth, L. Horesh, R. Bayford, and D. Holder, "Design and calibration of a compact multi-frequency EIT system for acute stroke imaging," *Physiological Measurement*, vol. 27, no. 5, pp. S199–S210, 2006, doi: 10.1088/0967-3334/27/5/S17.

[18] D. Y. Kim, H. Wi, P. J. Yoo, T. I. Oh, and E. J. Woo, "Performance evaluation of KHU Mark2 parallel multi-frequency EIT system," *Journal of Physics: Conference Series*, vol. 224, p. 012013(4pp), 2010, doi: 10.1088/1742-6596/224/1/012013.

[19] T. I. Oh, H. Wi, D. Y. Kim, P. J. Yoo, and E. J. Woo, "A fully parallel multi-frequency EIT system with flexible electrode configuration: KHU Mark2," *Physiological Measurement*, vol. 32, no. 7, pp. 835–849, 2011, doi: 10.1088/0967-3334/32/7/S08.

[20] M. Nahvi and B. S. Hoyle, "Wideband electrical impedance tomography," *Measurement Science and Technology*, vol. 19, no. 9, p. 094011(9pp), 2008, doi: 10.1088/0957-0233/19/9/094011.

[21] Y. Yang and J. Jia, "A multi-frequency electrical impedance tomography system for real-time 2D and 3D imaging," *Review of Scientific Instruments*, vol. 88, no. 8, p. 085110(12pp), 2017, doi: 10.1063/1.4999359.

[22] T. I. Oh, H. Koo, K. H. Lee, S. M. Kim, J. Lee, S. W. Kim, J. K. Seo, and E. J. Woo, "Validation of a multi-frequency electrical impedance tomography (mfEIT) system kHU Mark1: impedance spectroscopy and time-difference imaging," *Physiological Measurement*, vol. 29, no. 3, pp. 295–307, 2008, doi: 10.1088/0967-3334/29/3/002.

[23] E. Malone, G. Sato Dos Santos, D. Holder, and S. Arridge, "Multi-frequency electrical impedance tomography using spectral constraints," *IEEE Transactions on Medical Imaging*, vol. 33, no. 2, pp. 340–350, 2014, doi: 10.1109/TMI.2013.2284966.

[24] A. Romsauerova, A. McEwan, L. Horesh, R. Yerworth, R. H. Bayford, and D. S. Holder, "Multi-frequency electrical impedance tomography (EIT) of the adult human head: initial findings in brain tumours, arteriovenous malformations and chronic stroke, development of an analysis method and calibration," *Physiological Measurement*, vol. 27, no. 5, pp. S147–S161, 2006, doi: 10.1088/0967-3334/27/5/S13.

[25] Z. Xiao, C. Tan, and F. Dong, "Effect of inter-tissue inductive coupling on multi-frequency imaging of intracranial hemorrhage by magnetic induction tomography," *Measurement Science and Technology*, vol. 28, no. 8, p. 84001(11pp), 2017, doi: 10.1088/1361-6501/aa7504.

[26] Z. Cui, H. Wang, L. Tang, L. Zhang, X. Chen, and Y. Yan, "A specific data acquisition scheme for electrical tomography," in *Instrumentation and Measurement Technology Conference Proceedings*. IEEE, 2008, pp. 726–729, doi: 10.1109/IMTC.2008.4547132.

[27] T. K. Bera, J. Nagaraju, and G. Lubineau, "Electrical impedance spectroscopy (EIS)-based evaluation of biological tissue phantoms to study multifrequency electrical impedance tomography (Mf-EIT) systems," *Journal of Visualization*, vol. 19, no. 4, pp. 691–713, 2016, doi: 10.1007/s12650-016-0351-0.

[28] A. Chowdhury, T. K. Bera, D. Ghoshal, and B. Chakraborty, "Electrical impedance variantions in banana ripening: An analytical study with electrical impedance spectroscopy," *Journal of Food Process Engineering*, vol. 40, no. 2, p. e12387(14pp), 2017, doi: 10.1111 /jfpe.12387.

[29] J. Chen, L. Xu, Z. Cao, and H. Zhou, "Four-terminal imaging using a two-terminal electrical impedance tomography system," *IEEE Transactions on Instrumentation and Measurement*, vol. 63, no. 2, pp. 432–440, 2014, doi: 10.1109/TIM.2013.2280483.

[30] S. Liu, C. Tan, H. Wu, F. Dong, and J. Jia, "Wideband chirp excitation source for bioelectrical impedance spectrum tomography," in *International Instrumentation and Measurement Technology Conference*. IEEE, 2018, pp. 1 – 6, doi: 10.1109/ I2MTC.2018.8409539.

[31] IEC, "Medical electrical equipment part 1: General requirements for basic safety and essential performance," 2016.
[32] A. S. Tucker, R. M. Fox, and R. J. Sadleir, "Biocompatible, high precision, wideband, improved howland current source with lead-lag compensation," *IEEE Transactions on Biomedical Circuits and Systems*, vol. 7, no. 1, pp. 63–70, 2013, doi: 10.1109/TBCAS.2012.2199114.